Visualization of Concentration Gradients and Colloidal Dynamics under Electrodiffusiophoresis

Kun Wang,† Behrouz Behdani,† and Carlos A. Silvera Batista*,†,‡

†*Department of Chemical and Biomolecular Engineering, Vanderbilt University, Nashville, TN*

‡*Vanderbilt Institute for Nanoscale Science and Engineering*

E-mail: silvera.batista@vanderbilt.edu

Phone: (615) 875-6195

Abstract

In this work, we present an experimental study of the dynamics of charged colloids under direct currents and gradients of chemical species (electrodiffusiophoresis). In our approach, we simultaneously visualize the development of concentration polarization and the ensuing dynamics of charged colloids near electrodes. With the aid of confocal microscopy and fluorescent probes, we show that the passage of current through water confined between electrodes, separated about a hundred microns, results in significant pH gradients. Depending on the current density and initial conditions, steep pH gradients develop, thus becoming a significant factor in the behavior of charged colloids. Furthermore, we show that steep pH gradients induce the focusing of charged colloids away from both electrodes. Our results provide the experimental basis for further development of models of electrodiffusiophoresis and the design of non-equilibrium strategies for materials fabrication.

Introduction

Gradients in electrical potential (electric fields), along with gradients in concentration of ionic species, are important ways to control the motion of colloids. The surface and body forces[1,2] that electric fields exert on anisotropic colloids have opened new applications in self-propulsion,[2] transport of cargo,[3] dynamic assembly,[4] and directed assembly.[5,6] Similarly, diffusiophoresis (DP)—the motion of colloids induced by gradients of chemical species—has catalyzed the field of active colloids,[7,8] with profound implications in our understanding of the collective behavior of colloidal materials.[9–13] More specifically, strategies involving chemical gradients currently underlie efforts to purify water,[14,15] separate colloidal particles,[16] deliver drugs effectively,[17] and improve flow through porous media.[18,19] In biology, concentration gradients determine cellular communication, quorum sensing and chemotaxis.[20–23] Independently, motion via these two gradients, electrophoresis and DP, is well understood. However, motion generated from the combination of these two gradients is considerably less studied and offers another potentially useful mode of transport for the manipulation of colloidal systems.[24–26]

The current density (i_d) in an electrochemical cell results from the convection, diffusion and electromigration of ionic species,

$$I_d = Fu \sum z_i n_i - F \sum z_i D_i \nabla n_i + \sigma \nabla \phi, \tag{1}$$

where F, u, ϕ and n_i are the Faraday constant, the fluid velocity, electrical potential and concentration of ions; z_i, D_i and σ are the valence, diffusivity of ionic species and conductivity, respectively.[27] In the absence of chemical gradients and convection, the passage of an electrical current through a liquid electrolyte results in uniform electric fields ($E = -I_d/\sigma$) that drive the motion of charged particles under electrophoresis (EP). The slip velocity for a thin double layer with small zeta potentials is given by the Smolowchowski equation ($V_{EP} = \frac{\epsilon \zeta E}{\eta}$), in which the velocity of the particles (V_{EP}) is proportional to the zeta potential (ζ) and the electric field (E);[28,29] η and ϵ are the viscosity and dielectric constant of the medium. On the other hand, even in the absence of a current, gradients of ionic species of different diffusivity produce an electric field whose magnitude is given by $\nabla\phi = E = -\frac{F}{\sigma}\sum z_i D_i \nabla n_i$. Charged particles respond to such electric field by moving up or down the chemical gradient under diffusiophoresis. In the case of a binary electrolyte and thin double layer, the slip velocity under DP (V_{DP}) is given by,

$$V_{DP} = \frac{3}{2} D_B \left[\tilde{\zeta_p}\beta + 4\ln\left(cosh\frac{\tilde{\zeta_p}}{4} \right) \right] \nabla ln(n_0), \tag{2}$$

where $\tilde{\zeta} = (ze/k_bT)\zeta$ is the zeta potential scaled to the thermal voltage and $\beta = \frac{D^+ - D^-}{D^+ - D^-}$. D^+ and D^- are diffusivities of the positive and negative ions in the solution, and D_B is the diffusivity of a sphere with radius equal to the Bjerrum length.[30,31] Ultimately, a charged particle can move up or down a gradient depending on the sign of $\tilde{\zeta_p}\beta$ and the magnitude of the chemiphoretic term. In the presence of direct (or alternating) currents and concentration gradients, a charged particle will experience a combination of electrophoresis and diffusiophoresis: electrodifussiophoresis (EDP).

Out of the three electrokinetic phenomena (EP,[31,32] DP,[18,19,33–35] and EDP), EDP has been the least studied since the seminal work of Dukhin and collaborators.[24–26,36,37] In this sense and given significant advances in imaging, particle synthesis, surface modification and microfluidics since the early 80's, the study of EDP offers opportunities not only in fundamental research, but also in applied areas such as in the directed transport of colloids, fabrication of reconfigurable materials, and environmental remediation. For example, the closely related phenomenon of ion-concentration polarization (ICP) is used in microfluidics to focus, sort, and concentrate synthetic colloids[38–42] as well as biomolecules, such as DNA and proteins.[43,44] Similarly, ICP can be used in the desalination of water.[45] Although existing theories describe EDP for single particles with small or large zeta potentials,[24–26,37] possibilities for fundamental contributions exist in the context of dynamic assembly and manipulation of colloids near electrodes.[46] For example, pH gradients generated in the vicinity of planar electrodes led to the patterning of particles.[47]

In another key example, Silvera Batista et al. observed that when charged particles of low zeta potential were subjected to dc fields in DMSO, particles focused tens of microns away from both electrodes.[48] This puzzling observation hinted at the appearance of another force, whose magnitude could balance the electrophoretic force. The authors hypothesized that EDP caused the observed focusing, and that the gradients of electroactive species stablished by the passage of current were responsible for an additional diffusiophoretic force. However, it has not been possible to test this hypothesis, mainly, because of the lack of methods to visualize and quantify particle dynamics simultaneously with gradients of electroactive species—a general roadblock in the study of EDP. This task was particularly challenging to perform in DMSO due to its complex electrochemistry. In the fields of electrokinetics and directed assembly, gradients of electrochemical species near electrodes are rarely considered as an important factor, but previous studies point to significant effects on colloidal crystallization.[46]

In this paper, we propose a strategy to advance the study of EDP. First, we use a more tractable electrochemical medium (water in this case). As a medium, water offers the possibility to study many known electrochemical reactions. An interesting subset are those reactions that result in pH gradients due to the production or consumption of hydronium (hydroxide) ions, such as the electrolysis of water. Second, we monitor the products of electrochemical reactions or pH—simultaneously with the electrokinetic response of charged particles—using Laser Scanning Confocal Microscopy (LSCM). LSCM has enabled the visualization of electrochemical systems in-operando, therefore facilitating the study of reaction mechanisms and transport phenomena.[49–53] Third, to extract quantitative information from the measurements of fluorescence, we employ ratiometric analysis. Ratiometric analysis offers a reliable strategy to map local pH with high spatiotemporal resolution by accounting for inherent variability in emission intensity, caused by scattering, probing depth, and photobleaching of fluorescent probes. We have chosen SNARF-1 as the fluorescent pH indicator because its ratiometric properties do not significantly depend on its concentration or the ionic strength of the suspending medium.[54]

Herein, we present an experimental study of the dynamics of charged colloids under electrodiffusiophoresis. We study the response of fluorescent particles with tunable surface charge, under different current densities, initial pH and concentration of background electrolyte. The results demonstrate that the passage of current through water confined between transparent electrodes—separated by ≈ 120 μm—results in significant pH gradients. These large gradients, we argue, alter the forces experienced by charged particles and induce their focusing away from both electrodes. Qualitative analysis, based on the theory of diffusiophoresis for multicomponent systems, offers insight into the origin of the forces leading to focusing. Our results provide the experimental basis for the development of models of electrodiffusiophoresis that can enable the design of non-equilibrium strategies for materials fabrication.

Experimental Methods

The model systems in this study were fluorescent polystyrene particles with carboxylate surface groups (CB-PS) and nominal diameter of 1.0 μm (Bangs Lab, FCGB006). All particles were initially dispersed in ultrapure deionized water (18 MΩ·cm) with a volume fraction of approximately 1×10^{-3} %. Measurements of ζ were performed in a Litesizer 500 (Anton Paar) through electrophoretic light scattering. The CB-PS particles were negatively charged, with an average zeta potential (ζ) of -46.8 ± 1.1 mV. To change the ζ, particles were modified by cross-linking PEG chains of different molecular weights (5, 10, 20 and 30 kDa) to the carboxylate groups (PEG modified particles, PEG-PS), following the same procedure as in Reference 48. The attachment of PEG chains results in particles with less negative ζ, with the magnitude of the change modulated by the molecular weight of PEG molecules. For example, ζ for the 30 kDa PEG-PS particles was -28.8 ± 1.1 mV in contrast to -43.2 ± 2.3

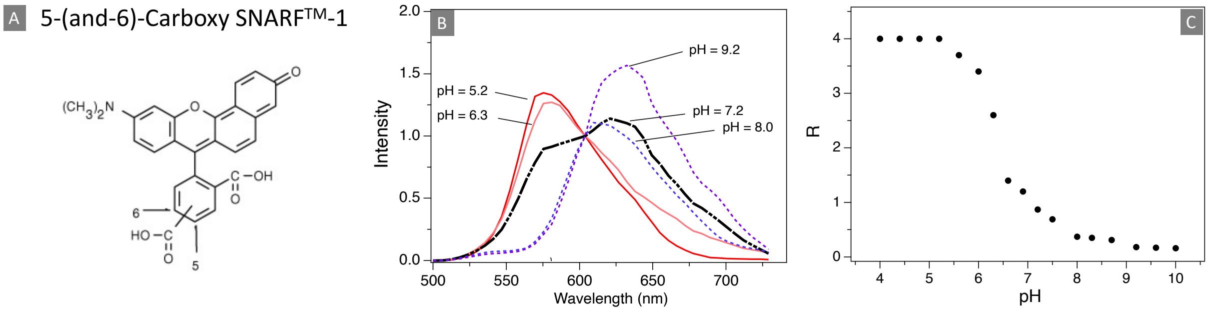

Figure 1: A) Molecular structure of carboxy SNARF-1. B) The emission spectrum of SNARF-1 changes with pH; the graphs shows the normalized emission intensity at different pH. C) The ratio R between emission at 580 nm and 640 nm decreases at higher pH; R provides the mean to probe the pH of aqueous media.

mV for 5 kDa PEG-PS particles.

The devices (electrochemical cells) were built by confining $\approx 20\mu$L of suspension between two ITO-coated glass slides (SPI supplies, 70-100 Ω) that are separated by a dielectric spacer with nominal thickness of 120 μm (9 mm, Grace Biolabs, Cat. # 654002). The ITO coatings are positioned so as to be in contact with the water. The slides were cleaned by sequentially sonicating in acetone, isopropanol and DI water for 10 min in each solvent. Then, right before assembly of the devices, the slides were exposed to a UV-ozone treatment (UVO Cleaner Model 30, Jelight) for 5 min. The electric fields were applied by connecting the device to a potentiostat operated in galvanostatic mode. Current densities ranged from 0.15 to 4.5 A/m^2. Imaging of the particles and the concurrent pH gradients was performed using a Leica SP8 confocal laser scanning microscope (CLSM) with 40×, 1.10 NA, water immersion objective and the pinhole set to 1 Airy unit. Multi-channel detection enabled the simultaneous imaging of the emission from particles and pH indicator, as well as the reflection from the bottom and top electrodes. Nonetheless, reflection mode was mainly used to check the exact position of the electrodes. The optical properties of the particles and ratiometric dye (SNARF™-1) were selected so their emission did not overlap. The particles were excited at 405 nm and their emission was collected between 420 and 450 nm. A high-speed resonant scanner (8 kHz) enabled high acquisition rates of up to 28 frames per second, at 512 × 512 pixel resolution.

5-(and-6)-carboxy SNARF™-1 (ThermoFisher, C1270) is an organic molecule whose fluorescence emission changes from yellow-orange at acidic pHs to deep red at basic pHs, Figure 1A. The ratiometric capabilities of SNARF stems from the different emission properties of the protonated and deprotonated species.[54] Deprotonation of the phenolic substituent of SNARF-1 shifts the emission from 583 nm to 627 nm, which enables the measurement of the relative concentration of the protonated and deprotonated species, Figure 1B. In the ratiometric method, the pH of the medium is linked to the dissociation equilibrium of the dye—characterized by the dissociation constant (pKa)—using the following formula:[55]

$$\text{pH} = \text{pKa} - log\left(\frac{R_b - R}{R - R_a} \cdot \frac{I_{b,2}}{I_{a,2}}\right), \tag{3}$$

where R is the ratio of intensities at two detection points, I_1 and I_2, while R_b and R_a are the ratios of intensities at the basic (I_b) and acidic (I_a) end points. Using the ratio of signals at two different wavelengths, minimizes the effect of fluctuations in focus, excitation intensities and concentration of the dye. In our experiments, SNARF (100 μM) was excited at 514 nm, while the emission windows for I_1 and I_2 were centered at 580 nm and 640 nm. All the experiments were performed with the same settings, using a detection window of 5 nm for the two detectors. For the calibration, we measured values for the pKa of carboxy SNARF-1 very similar to those reported by the vendor (≈ 7.3), whereas the acidic and basic end points were measured at approximately pH 9 and 4, respectively. The measurements of pH in this work were performed within the limits of the end-points. Images were converted to pH maps using an algorithm developed in Igor Pro. The algorithm relies on the calibration data and Equation 3. The experiments with sodium fluorescein, another pH sensitive dye, follow a similar procedure as when using SNARF-1, with the necessary adjustments for excitation and emission wavelengths.

Results

This section presents the results from experiments aimed at visualizing the pH gradients induced by electrolysis over length scales of a hundred microns. Next, the effect of two key parameters—current density and initial pH—is discussed. Subsequently, the focus shifts to study the response of charged particles to the electrochemical conditions within the cell.

Visualization of pH gradients. The 3D confocal images in Figure 2A-C show the volume within the electrochemical cell before and after applying a current density equal to 4.5 A/m^2 through an aqueous medium containing SNARF-1. The images show the view from the x-z plane of the volume between the electrodes. Although not shown, the electrodes are located immediately below and above the colored section, as the scheme in Figure 2D illustrates. The images combine the intensity collected at 580 nm (I_1, yellow) and at 640 nm (I_2, red). Initially, the color throughout the cell is uniform, indicating a constant pH at the value of $\approx$ 7.2. When the current is applied between the cathode (top electrode) and anode (bottom electrode) for 65 s, the ratio of intensity ($R = I_1/I_2$) from the two detection channels changes. The intensity collected at the red channel becomes much higher near the cathode ($R \approx 0.4$), while it decreases near the anode ($R \approx 2.6$), in comparison to an initial $R \approx 1$. The lower value of R near the cathode indicates an increase in pH, while the opposite occurs near the anode. Analysis based on Equation 3 reveals the pH ranges from approximately 8.5 to 6.5. The system is dynamic since the zone of basic pH spans half the cell after 104 s. To summarize, the images demonstrate that significant and measurable pH gradients form within the electrochemical cell with the passage of current.

The qualitative results follow the trends expected from the electrolysis of water (Figure 2D). At the cathode, reduction of water occurs, resulting in the evolution of hydrogen and the formation of hydroxide ions. In contrast, at the anode, oxidation of water takes place, resulting in the evolution of oxygen and the formation of hydronium ions. Consequently, as the electrical current passes through the cell, the accumulation of hydroxide ions near the cathode and hydronium ions near the anode results in basic and acidic pHs, respectively. Experiments with another pH sensitive dye, fluorescein, also show two distinct zones, one where the emission is quenched (indicating acidic pH) and another where the intensity increases (indicating basic pH). Although the pKa of SNARF-1 and fluorescein are different, the ex-

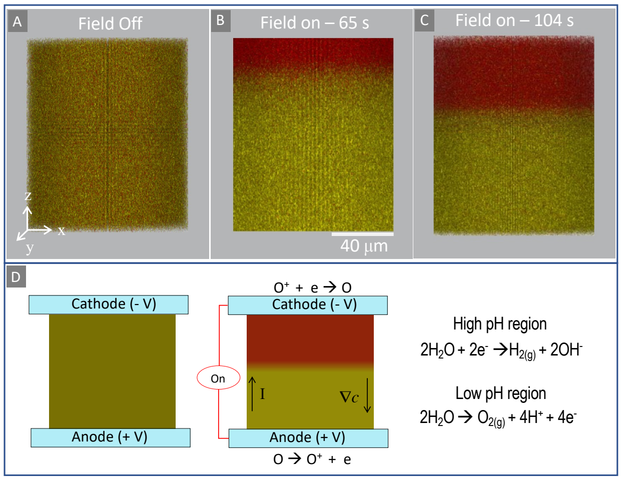

Figure 2: Imaging of the emission from SNARF-1 through confocal microscopy enables the visualization of pH gradients during electrolysis of water. A-C) Confocal images of the volume between the electrodes before and after applying a current density of 4.5 A/m^2 for 65 and 104 seconds. D) Schematic of the device (electrochemical cell) and accompanying reactions for a typical experiment. The reduction and oxidation of water leads to regions of higher and lower pH, respectively, in comparison to the initial value of ≈ 7.2. The images report volumes of cross sectional area equal to 106×106 μm^2, electrode gap of 120 μm and detection from two channels at 580 nm (yellow-orange) and 640 nm (red).

perimental results in Figure 2 and S1 suggest general features about the electrochemical behavior of the system.

Modulation of pH gradients through current density and initial pH. Current density and initial pH are two readily available parameters to set the electrochemical conditions within the experimental cells. To better appreciate the evolution of the system, the first row in Figure 3 shows heat plots that condense the temporal and spatial distribution of pH during a single experiment, while the second row shows the pH profile for a single time (53 seconds), denoted by the black-dashed lines in the respective heat plot. The values of pH reported in the heat plots were calculated using Equation 3 and the ratio of intensities from the two detection channels, after image analysis and processing of data through a routine in Igor Pro. The color scales in these plots range from bright red (pH 6) to bright blue (pH 9).

The panels in Figure 3 show the response of the system to different current densities (0.15, 0.2, 0.5, and 4.5 A/m^2). For the lowest current density (0.15 A/m^2), the map and profile at 53 seconds indicate the pH does not change significantly from the initial value (≈ 7.2) throughout an experiment. As the current density increases to 0.2 A/m^2 (Fig. 3B and 3F), the pH remains relatively uniform during the first half of the experiment. However,

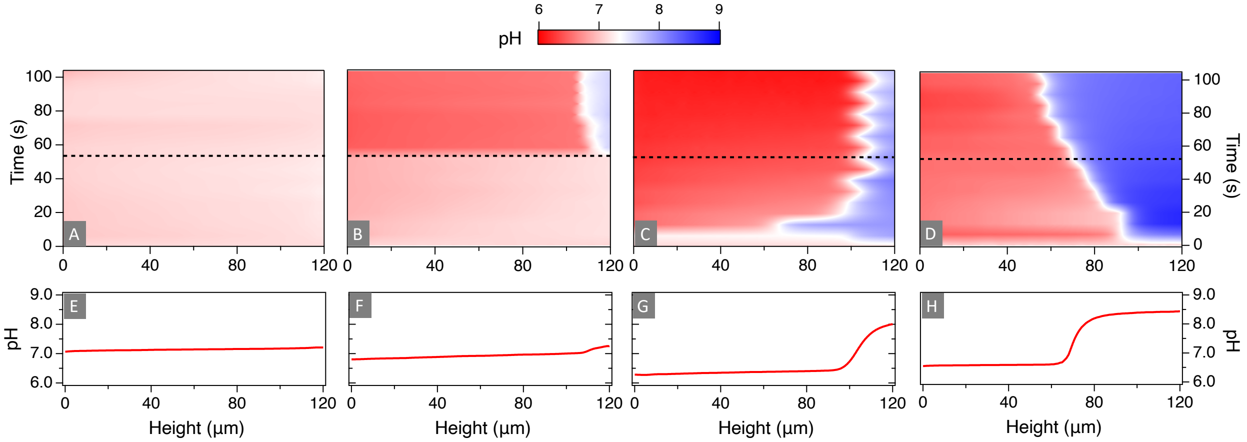

Figure 3: The value of current density impacts the observed pH profiles. Panels (A-D) are 2D heat maps that condense the pH profiles for all times in a single experiment, while panels (E-H) represent the pH profile for a single time (52 s), indicated by the dashed lines. The applied current densities were 0.15 (A,E), 0.2 (B,F), 0.5 (C,G) and 4.5 (D,H) A/m^2.

after 53 s, the pH begins to increase rapidly near the cathode, and a clear region of basic pH develops, as evidenced by the light blue color. When 0.5 A/m^2 is applied, clear regions characterized by acidic and basic pHs develop soon after turning on the electric field (Fig. 3C). The profile in Figure 3G shows the pH decreases below 7 near the anode, but it begins to increase slowly towards the cathode until there is a jump to values that plateau near 8. The process is dynamic; initially the basic region extends 50 μm into the cell, but it steadily decreases in size until becoming 20 μm in width, by the end of the experiment. At the current density of 4.5 A/m^2(Fig. 3D), the plot shows that two diffusion fronts, one acidic and the other basic, form from the anode and cathode, respectively. Interestingly, the position at which the two diffusion fronts meet results in a noticeable sudden change in pH that resembles a Sigmoidal function (Fig. 3H). These results demonstrate that, depending on the experimental parameters, significant concentration polarization occurs within the whole electrochemical cell, not only close to the electrodes. It is important to notice that the Sigmoidal shape of the profile is not due to the limitations of the dye since the measured values were ensured to be safely between the acidic and basic endpoints.

In addition to current density, the formation of two distinct acidic and basic regions also depends on the starting pH of the solution (pH$_\text{i}$). While the maps for pH$_\text{i}$ 7.2 and 8.5 contain distinct regions of basic and acidic pHs, those for pH$_\text{i}$ 6.5 remain uniform throughout the experiments (Figures S2 and S3). Therefore, the trends in these experiments suggest the distinct regions of pH form more easily when the pH_i is basic or close to neutral.

Response of charged particles under EDP. To study the behavior of charged particles under the generated electrochemical conditions, the fluorescence intensity from PEG-PS particles and from the SNARF-1 were recorded simultaneously, as a current density flowed through the system. Particles were selected with emission and excitation that do not overlap with those of SNARF; therefore, our model system has an emission peak at 440 nm, with excitation at 405 nm. Experiments at different current densities illustrate the effect of pH gradients on the response of particles. Figure 4 compares maps of fluorescence intensity from particles (30 kDa PEG-PS), for all times in a single experiment. The corresponding pH maps (Figure S4-S5) resemble those already described in Figure 3, suggesting that at the low volume fraction used in these experiments, the pH profile is not significantly affected by the presence of the particles. In the intensity maps, the white color indicates the highest relative intensity—and consequently, concentration of particles—while the dark blue indicates the lowest relative intensity. At the lowest current density (0.15 A/m^2), the intensity from the particles progressively increases at the bottom, indicating unidirectional motion towards and accumulation at the anode. The profile in Figure 4C shows that, after 86 seconds, emission intensity is five times higher at the anode in comparison to the cathode.

The response of the particles under 4.5 A/m^2 is remarkably different; particles migrate away from both electrodes, and after 40 seconds, they focus in a narrow band (see intensity profile Fig. 4D). Most importantly, comparing the pH (Fig. S5) and intensity maps (Fig. 4), as well as the images in Figure 5, it is evident that particles accumulate exactly at the position where the steepest change in pH occurs. The peaks in the intensity maps trace the same trajectory as the boundary between the regions of basic and acidic pH. Also, particles move more easily down the gradient of pH (from cathode to anode) than up the gradient (from anode to cathode). Consequently, the concentration of particles is usually higher near the anode. The data in Figure 4, and the corresponding images, suggest the focusing of

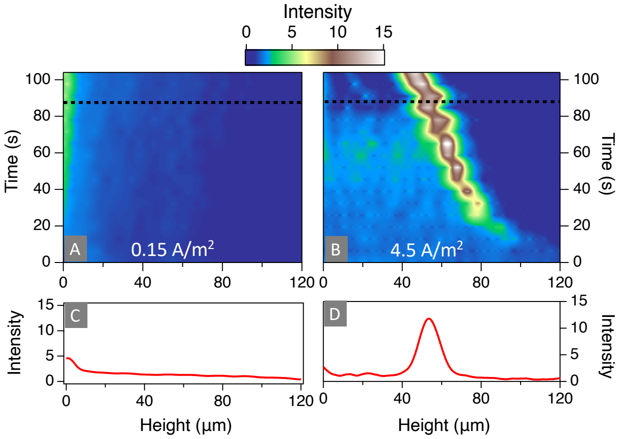

Figure 4: The current density and the accompanying pH gradients determine the response of charged particles. Panels (A-B) are 2D heat maps that condense the fluorescence intensity from the particles for all times in a single experiment, while Panels (C-D) represent the intensity profile for a single time (86 s). The applied currents were 0.15 (A,C) and 4.5 (B,D) A/m^2, while the average zeta potential of the particles (30 kDa PEG-PS) was -28.8 ± 1.0 mV. Figures S4 and S5 show that the respective pH profiles are similar to those measured in the absence of particles, Figure 3.

particles results from the steep pH gradients produced by the electrolysis of water. Even at high currents, if a steep pH gradient does not form (see the case for pHi 6.5 in Fig. S3), particles do not experience focusing. Focusing is generally observed when current densities above 0.9 A/m^2 are applied. Later, we will see that the presence of steep pH gradients is a necessary, but not a sufficient condition, to achieve significant accumulation of particles away from the electrodes. It is worth noting that the accumulation of particles increases the scattering of excitation light, thus decreasing the emission intensity from SNARF-1 above the focusing point (Figure 5). Nonetheless, the ability to account for such variations in intensity—since it does not rely on absolute intensity—constitute an important advantage of using ratiometric analysis. These experiments show that particles respond appreciably to both the electric fields and the concentration gradients generated by the electrochemical reactions that sustain the passage of current.

The permanent surface charge of the particles strongly impacts their response under EDP. Figure 6 shows intensity maps for particles of different zeta potential under 4.5 A/m^2, and consequently, in the presence of pH profiles similar to those in Figures 3 and S5. The particles with the highest zeta potential (-46.8 ± 1.1 mV) rapidly accumulate away from the electrodes, but the focused band of particles drifts downwards and away from the point where

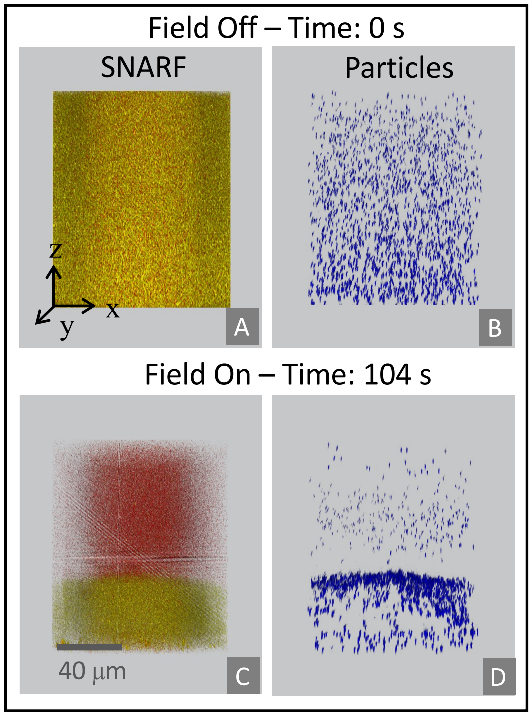

Figure 5: Simultaneous imaging of SNARF-1 and charged particles enables linking electrokinetic response to the developing pH gradients. The images correspond to the experimental data represented in Figure 4 at the beginning (A-B) and at the end of the experiment (C-D). The images report volumes of cross section area equal to 106 × 106 μm^2, electrode gap of 120 μm and detection from three channels centered at 435 nm (blue), 580 nm (yellow-orange) and 640 nm (red).

the maximum gradient in pH occurs. Eventually, after 50 seconds, all particles deposit on the anode. As the zeta potential increases to -43.2 ± 2.3 mV, particles do not move upwards as readily, but all particles deposit on the anode, like in the previous case. Once the zeta potential increases to -34.6 ± 1.6 mV (10 kDa PEG-PS), particles accumulate at the position where the largest gradient in pH is taking place—that is, at the boundary between the basic and acidic zones—although a portion of them remained dispersed in the region near the anode. As the zeta potential increases further (-31.9 ± 1.0 mV, 20 kDa PEG-PS), particles move upwards more readily, and as a result, most of the particles join the focused band at the end of the experiment. Even when a high current is applied and a large pH gradient is induced, particles' response depends on the zeta potential, and their behavior falls in the spectrum from deposition to focusing far from the electrodes. If focusing is the desired outcome of an experiment, in addition to the presence of a large pH gradient, particles must have low enough zeta potential to move easily down and up the pH gradient.

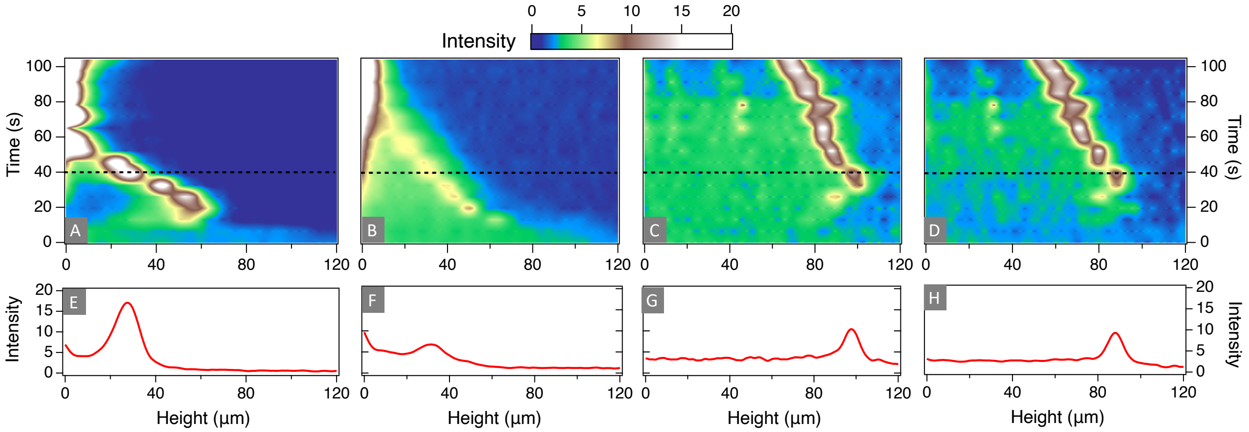

Figure 6: The rate of migration towards the position of steepest pH gradient increases as absolute zeta potential decreases. Panels A-D are 2D heat maps that condense the fluorescence intensity from the particles for all times in a single experiment, while Panels E-H represent the intensity profile for a single time (40 s). The average zeta potential for the samples was -46.8 ± 1.1 (A,E), -43.2 ± 2.3 (B,F), -34.6 ± 1.6 (C,G) and -31.9 ± 1.0 (D,H) mV. Th

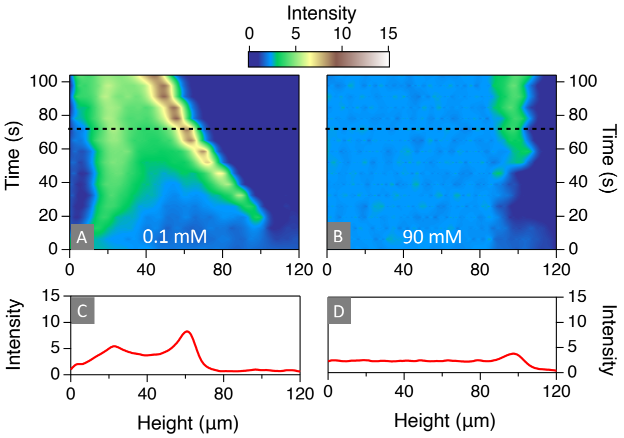

Figure 7: The concentration of background electrolyte dampens the effect of pH gradients. Panels A-B are 2D heat maps that condense the fluorescence intensity from the particles for all times in a single experiment, while Panels (C-D) represent the intensity profile for a single time (72 s). The applied current was 4.5 A/m^2, while the average zeta potential of the particles (30 kDa PEG-PS) was -28.8 ± 1.0 mV.

Concentration of a background electrolyte constitute another important variable to control the response of particles. The background electrolyte affects both electrochemical conditions and electrokinetic response of the particles, first by changing the distribution of current among the ions, and second, by setting the Debye length. We chose NaSCN as a supporting electrolyte because, for the range of concentrations in the experiments, it did not change the zeta potential of the particles substantially; at 90 mM NaSCN, the zeta potential for 30 kDA PEG-PS particles changed from -28.8 ± 1.0 to -23.0 ± 1.1 mV. In contrast, NaNO$_3$ adsorbs to polystyrene particles due to ion-specific effects, which leads to substantial changes in zeta potential.[56] In this case, the zeta potential increased to -5.4 ± 1.0 at 90 mM NaNO$_3$. At 0.1

mM NaSCN, which sets the Debye length to 30 nm, particles move rapidly from the cathode to the anode and accumulate at the position of maximum pH gradient (Fig. 7A). On the other hand, particles closer to the anode move upwards. As a result, Figure 7C shows the particles accumulate into one broad peak close to the anode, and on a another one, at the point where gradient is steepest. Increasing the concentration of NaSCN to 90 mM, which sets the Debye length to 1 nm, induces a significant change in the response of the particles; the velocity of the particles decreases substantially, to the extent that accumulation is minimal at any point within the cell. However, some particles do focus close to the cathode by moving downwards at a rate of approximately 0.4 μm/s. The slight accumulation of particles 20 μm below the cathode is a manifestation of the different distribution of pH at higher concentrations of NaSCN, see Figure S7 for the corresponding pH maps.

Discussion

Ratiometric analysis and fast imaging with LSCM enables the visualization of local pH and particle distributions with high resolution in space and time. This approach overcomes important challenges related to changes in transmittance of the conductive slides, photobleaching of the dye and changes in intensity due to scattering from the particles. For the range of applied current density (0.15 - 4.5 A/m^2), pH gradients are substantial. For example, when a current of 4.5 A/m^2 is applied, pH changes by more than two units from the anode to the cathode. Using CLSM and a variety of pH sensitive dyes (fluorescein, LysoSensor, carboxynaphtho-fluorescein, and BCECF), other works have reported similar changes in pH near electrodes—after applying a wide range of current densities (0.1-1600 A/m^2) to effect water electrolysis.[51–53,57] A distinctive feature of the results in Figure 3 is the shape of the pH profile; when current densities above 0.5 A/m^2 are applied, pH does not change smoothly from anode to cathode. Instead, there was a sharp transition from acidic to basic regions.

A simplified model provides insight about the pH profile within the cell. We solve the Poisson-Nernst-Planck equations in the liquid domain for the OH^-, H^+ and SNARF-1 species,

$$\frac{\partial n_i}{\partial t} + \nabla \cdot \mathbf{j}_i = R_j, \tag{4}$$

$$\mathbf{j}_i = -D_i \nabla n_i - n_i \mu_i \nabla \phi + n_i \mathbf{u}, \tag{5}$$

with the mobilities given by the Einstein-Smoluchowski equation, $\mu_{\pm} = D_{\pm} ez/k_B T$. The model solves the transient equation for conservation of ionic species.[46,58,59] Diffusion, migration and convection determines the flux, $\mathbf{j}_i$, of ionic species. The reaction term, R_i, accounts for the equilibrium reaction of water ($2\,H_2O \rightleftharpoons H^+ + OH^-$) and dissociation of SNARF ($SNARF^{-1} \rightleftharpoons SNARF^{-2} + H^+$) within the liquid domain. The dissociation equilibrium of the SNARF molecules occurs between species holding either one or two net negative charges.[60] The electroneutrality condition applies in the liquid domain since the size of the electrical double layer is of the order of tens of nanometers. As a first step, the model does not describe the electrode kinetics. Therefore, the exact potential drop at the electrode, and consequently, the potential within the electrolyte are not known. Instead of modeling the electrode kinetics, the voltage in the electrolyte is accounted for as an externally imposed parameter. Given the low conductivities in our experiments, it is important to include the migration term. On the other hand, constant fluxes at the boundaries account for the reactions at the electrodes. Water electrolysis constitutes the most dominant Faradaic reaction in the system, which produces protons at the anode and hydroxyl ions at the cathode, when carried out at neutral pHs:

Anode: $2\,H_2O \rightleftharpoons O_2 + 4\,H^+ + 4\,e^-$

Cathode: $4\,H_2O + 4\,e^- \rightleftharpoons 2\,H_2 + 4\,OH^-$.

Therefore, the boundary conditions at the anode are: $\mathbf{j}_{H^+} = \frac{I_d}{F}$, and $\mathbf{j}_{OH^-} = 0$, while at the cathode they are $\mathbf{j}_{OH^-} = \frac{I_d}{F}$, and $\mathbf{j}_{H^+} = 0$. While it is not possible to keep both the current and the potential constant in a real experiments, this strategy provides approximations to the behavior of the system. The coupled equations were solved using the finite element method as implemented in COMSOL Multiphysics, using the modules for the transport of dilute species and the tertiary current distribution.

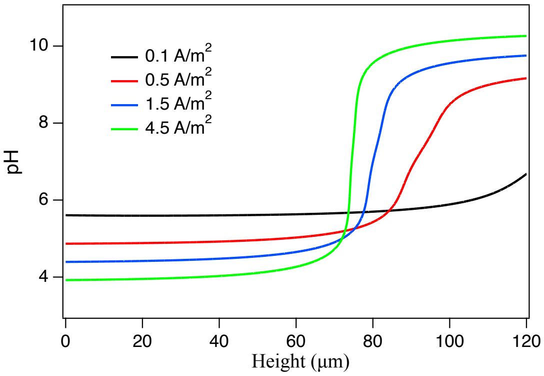

Figure 8: Solution of the Poisson-Nernst-Planck equations captures the dependence of pH profile with current density. The graph shows the pH profiles at steady state for each current density. The Sigmoidal pH profile emerges when the current density reaches values close to 0.5 A/m^2, which is in agreement with the experimental observations in Figure 3.

Figure 8 shows the steady state pH profile within the liquid domain after applying current densities between 0.1 and 4.5 A/m^2. At low current densities, the pH increases towards the cathode, similar to what is observed in the experiments. As the current density increases, the Sigmoidal shape of the pH profile emerges. When $I_d = 0.5$ A/m^2, the pH profile shows acidic and basic regions, with a sharp gradient at 90 μm. The model did not account for convection due to changes in buoyancy. However, low ionic conductivity and absence of dense ions limit the effects of buoyancy. In fact, convective transport due to changes in buoyancy throughout the cell will reduce the likelihood that such profile will form, as detailed in the recent work by Obata et al. Therefore, the observed pH profiles result from the transport due to diffusion and migration. Nonetheless, there are noteworthy discrepancies between the experimental results and the predictions from the model. First, the range of values is wider in the model. The model predicts pH values near the anode that are at least one unit lower than the experimental values. In the model, steady state is reached rapidly, within 10 s. However, in the experiments, the profile continuously evolve and only levels off after 80 seconds. These differences presumably stem from not accounting for the electrode kinetics and other possible reactions.

The experimental results in Figures 4 and 5 show that a reproducible point of zero velocity, and therefore focusing, occurs at the transition from acidic to basic regions. Consequently, the point of highest particle concentration coincides with the position at which the gradient in pH is largest. The lack of focusing in the absence of pH gradients—either when using a buffer or when the starting pH is highly acidic, see SI—confirms the hypothesis that electrochemically generated gradients of ionic species are needed to effect focusing of charged particles under uniform electric fields. When gradients of redox species are superimposed to electric fields, electrodiffusiophoresis governs the transport of particles.[24] Focusing of charged particles under electrodiffusiophoresis has been reported using ion-selective membranes,[26,48] although direct visualization of electroactive species was not presented. Dukhin and collaborators observed that particles accumulated away from ion-selective membranes and formed non-equilibrium structures, which they termed “fluid deposits”.[26] In their experiments, the fluid velocity tangential to the surface of the membrane set the thickness of the diffusion layer, and therefore, the position of focusing.

An alternative mechanism to explain the behavior of particles is isoelectric focusing (IEF). In IEF, particles migrate under the influence of an electric field and across a pH gradient until they reach their point of zero charge. IEF requires that particles hold negative, as well as positive charges. Though the carboxylate-polystyrene particles show zero charge at low pH ($\sim$3), they do not acquire positive charges at any of the observed pHs, consequently ruling out IEF as the mechanism. Dielectrophoresis is another potential mechanism; however, since the applied electric field is uniform in our experiments, the dielectrophoretic force does not provide a significant contribution.

As a first approximation, EDP can be described by the addition of an electrophoretic and a diffusiophoretic term:[26]

$$V_{EDP} = V_{EP} + V_{DP}. \tag{6}$$

For a thin double layer, V_{EP} is given by the Smolowchowski equation, so for negatively charged particles, V_{EP} points towards the anode. As a result, the upward velocity needed to observe focusing must stem from the V_{DP} term. V_{DP} can be directed towards the anode or the cathode depending on the zeta potential, as well as the diffusivity and gradients of ionic species. Since more than two ions are present in the system, the theories developed for binary electrolytes—such as Equation 2—do not apply, but a qualitative analysis is possible using a theory recently developed by Squires and collaborators for multicomponent systems.[61] The theory provides an expression for V_{DP} that depends on the fluxes (j_i), the diffusivity of the ions (D_i) and the zeta potential ($\widetilde{\zeta_p}$):

$$V_{DP} = \frac{k_B T}{n_0^B}\left(M_+ \sum_+ \frac{j_i}{D_i} + M_- \sum_- \frac{j_i}{D_i}\right), \text{with} \quad - M_\pm = \frac{\varepsilon}{e\eta}\frac{k_B T}{2e}\left[\mp\widetilde{\zeta_p} + 4ln\left(cosh\frac{\widetilde{\zeta_p}}{4}\right)\right]; \tag{7}$$

n_0^B represents the bulk electrolyte concentration. To calculate V_{DP}, the fluxes for all species must be known.

The theory reveals there are two important physical conditions that must be met in order to achieve focusing through pH gradients and diffusiophoresis. First, the concentration profile must be divergent. Particles accumulating away from the electrodes must experience positive and negative V_{DP}, which implies having different fluxes on either side of the focusing point, according to Equation 7. A change of sign in V_{DP} is possible when divergent fluxes ($\nabla \cdot j_i \neq 0$) are established due to reactions—ionic, dissociative or aggregative.[61] The Nernst-Planck equations provide the fluxes of charged species by adding contributions from diffusion, electromigration and convection. Except near the electrodes, the electrical potential will vary linearly with distance, and therefore its second derivative will be zero throughout the cell. Consequently, in the absence of convection, a finite divergence implies $\nabla \cdot \mathbf{j_i} \sim \frac{\partial^2 n_i}{\partial x^2} \neq 0$. The profiles for the experiments at 4.5 A/m^2 and pHi 7.2 confirm the fluxes for H$^+$ and OH$^-$ are indeed divergent, since the second derivatives of the concentration profiles are nonzero. The relevant reactions are the Faradaic reactions at the electrodes and the dissociation of water.

The second constraint involves the diffusivities of H^+ and OH^- and the zeta potential of the particles,

$$\frac{D_{OH^-}}{D_{H^+}} < \frac{\widetilde{\zeta}_p + 4ln\left(cosh\frac{\widetilde{\zeta}_p}{4}\right)}{\widetilde{\zeta}_p - \ 4ln\left(cosh\frac{\widetilde{\zeta}_p}{4}\right)}. \tag{8}$$

All of the particles used in the experiments comply with the second criterion. Although the particles with the highest zeta potential show a mixed behavior of focusing and deposition, experiments in Figure 6 follow the trends predicted, where focusing becomes less likely as the zeta potential increases. In addition, calculations of velocity (see SI, Figure S8) using Equations 6 and 7 show that points of zero velocity do emerge far from both electrodes, leading to focusing. As a summary, the pH profiles that are produced electrochemically in our experiments fulfil the conditions necessary to induce focusing in charged colloidal particles, according to the theory of diffusioresis for multicomponent systems.

The experimental results demonstrate that measurable gradients in pH induce motion that balance and counteract traditional electrophoretic motion. Except for the seminal work of Dukhin,[26,36] and a few recent—theoretical[24,25,37,62,63] as well as experimental[46,47]—studies, most treatments of colloidal electrokinetics ignore the effects of electrochemically induced gradients. Therefore, by providing the means to simultaneously map concentration gradients and the ensuing colloidal dynamics, this work provides tools to further the understanding of charged particles under electric fields, especially near electrodes.[64–66] On the other hand, EDP has potential for performing practical tasks in lab-on-a-chip devices such as focusing, trapping and separations.

Conclusions

The strategy presented in this paper allows the simultaneous visualization and quantification of local pH and colloidal dynamics within the electrochemical cells. Fast imaging with LSCM enables visualization of pH and particle distributions with high resolution in space and time.

The measurements of pH reveals the formation of steep gradients when currents between 0.15 and 4.5 A/m^2 are applied to electrochemical cells with characteristic size of approximately 100 μm. Images of charged fluorescent particles and pH sensitive dye show that particles accumulate at positions where the pH gradients are largest. Qualitative analysis supports the hypothesis that focusing of particles away from the electrodes is mainly due to the diffusiophoretic contribution by the electrochemically generated pH gradients. Future work will focus on using low frequency ac fields to modulate the pH profiles and to tune the potential landscape experienced by the particles. Therefore, future work will also explore the implications of EDP on directed assembly.

Acknowledgement

The authors thank Vanderbilt University for resources provided through start-up package. We also thank Keara Saud for providing valuable feedback on the manuscript.

Supporting Information Available

Additional pH and intensity maps for experiments at different initial pH and electrolytes. Images for experiments with fluorescein and calculations of velocity (V_{EDP}).

References

(1) Gangwal, S.; Cayre, O. J.; Bazant, M. Z.; Velev, O. D. Induced-Charge Electrophoresis of Metallodielectric Particles. *Physical Review Letters* **2008**, *100*, 058302.

(2) Ma, F.; Yang, X.; Zhao, H.; Wu, N. Inducing Propulsion of Colloidal Dimers by Breaking the Symmetry in Electrohydrodynamic Flow. *Physical Review Letters* **2015**, *115*, 208302.

(3) Boymelgreen, A. M.; Balli, T.; Miloh, T.; Yossifon, G. Active colloids as mobile microelectrodes for unified label-free selective cargo transport. *Nature Communications* **2018**, *9*, 760.

(4) Yan, J.; Han, M.; Zhang, J.; Xu, C.; Luijten, E.; Granick, S. Reconfiguring active particles by electrostatic imbalance. *Nature Materials* **2016**, *15*, 1095–1099.

(5) Shah, A. A.; Ganesan, M.; Jocz, J.; Solomon, M. J. Direct current electric field assembly of colloidal crystals displaying reversible structural color. *ACS Nano* **2014**, *8*, 8095–103.

(6) Shah, A. A.; Kang, H.; Kohlstedt, K. L.; Ahn, K. H.; Glotzer, S. C.; Monroe, C. W.; Solomon, M. J. Liquid Crystal Order in Colloidal Suspensions of Spheroidal Particles by Direct Current Electric Field Assembly. *Small* **2012**, *8*, 1551–1562.

(7) Córdova-Figueroa, U. M.; Brady, J. F. Osmotic Propulsion: The Osmotic Motor. *Physical Review Letters* **2008**, *100*, 158303.

(8) Howse, J. R.; Jones, R. A. L.; Ryan, A. J.; Gough, T.; Vafabakhsh, R.; Golestanian, R. Self-Motile Colloidal Particles: From Directed Propulsion to Random Walk. *Physical Review Letters* **2007**, *99*, 048102.

(9) Palacci, J.; Sacanna, S.; Steinberg, A. P.; Pine, D. J.; Chaikin, P. M. Living Crystals of Light-Activated Colloidal Surfers. *Science* **2013**, *339*, 936 940.

(10) Aubret, A.; Youssef, M.; Sacanna, S.; Palacci, J. Targeted assembly and synchronization of self-spinning microgears. *Nature Physics* **2018**, *14*, 1114–1118.

(11) Aubret, A.; Palacci, J. Diffusiophoretic design of self-spinning microgears from colloidal microswimmers. *Soft Matter* **2018**, *14*, 9577–9588.

(12) Ginot, F.; Theurkauff, I.; Detcheverry, F.; Ybert, C.; Cottin-Bizonne, C. Aggregation-fragmentation and individual dynamics of active clusters. *Nature Communications* **2018**, *9*, 696.

(13) Goodrich, C. P.; Brenner, M. P. Using active colloids as machines to weave and braid on the micrometer scale. *Proceedings of the National Academy of Sciences* **2017**, *114*, 257 – 262.

(14) Straub, A.; Deshmukh, A.; Elimelech, M. Pressure-retarded osmosis for power generation from salinity gradients: is it viable? *Energy & Environmental Science* **2016**, *9*, 31–48.

(15) Shin, S.; Shardt, O.; Warren, P. B.; Stone, H. A. Membraneless water filtration using CO2. *Nature Communications* **2017**, *8*, ncomms15181.

(16) Abécassis, B.; Cottin-Bizonne, C.; Ybert, C.; Ajdari, A.; Bocquet, L. Boosting migration of large particles by solute contrasts. *Nature Materials* **2008**, *7*, 785–789.

(17) Joseph, A.; Contini, C.; Cecchin, D.; Nyberg, S.; Ruiz-Perez, L.; Gaitzsch, J.; Fullstone, G.; Tian, X.; Azizi, J.; Preston, J.; Volpe, G.; Battaglia, G. Chemotactic synthetic vesicles: Design and applications in blood-brain barrier crossing. *Science advances* **2017**, *3*, e1700362.

(18) Shin, S.; Um, E.; Sabass, B.; Ault, J. T.; Rahimi, M.; Warren, P. B.; Stone, H. A. Size-dependent control of colloid transport via solute gradients in dead-end channels. *Proceedings of the National Academy of Sciences* **2016**, *113*, 257–261.

(19) Kar, A.; Chiang, T.-Y.; Rivera, I. O.; Sen, A.; Velegol, D. Enhanced transport into and out of dead-end pores. *ACS Nano* **2015**, *9*, 746–53.

(20) Monast, C.; Furcht, C.; Lazzara, M. Computational Analysis of the Regulation of EGFR by Protein Tyrosine Phosphatases. *Biophysical journal* **2012**, *102*, 2012–21.

(21) Pinilla-Macua, I.; Watkins, S. C.; Sorkin, A. Endocytosis separates EGF receptors from endogenous fluorescently labeled HRas and diminishes receptor signaling to MAP

kinases in endosomes. *Proceedings of the National Academy of Sciences* **2016**, *113*, 2122–2127.

(22) Danino, T.; Mondragón-Palomino, O.; Tsimring, L.; Hasty, J. A synchronized quorum of genetic clocks. *Nature* **2010**, *463*, 326.

(23) Basu, S.; Gerchman, Y.; Collins, C. H.; Arnold, F. H.; Weiss, R. A synthetic multicellular system for programmed pattern formation. *Nature* **2005**, *434*, 1130.

(24) Rica, R. A.; Bazant, M. Z. Electrodiffusiophoresis: Particle motion in electrolytes under direct current. *Physics of Fluids* **2010**, *22*, 112109.

(25) Yariv, E. Communication: The phoretic drift of a charged particle animated by a direct ionic current. *The Journal of Chemical Physics* **2010**, *133*, 121102.

(26) Ulberg, Z. R.; Dukhin, A. S. Electrodiffusiophoresis - film formation in Ac and Dc electrical fields and its application for bactericidal coatings. *Progress in Organic Coatings* **1990**, *18*, 1–41.

(27) Newman, J. S. *Electrochemical systems*, 3rd ed.; Wiley: Hoboken, N.J., 2004.

(28) von Smoluchowski, M. *Elektrische Endosmose und Strömungsströme*; J.A. Barth: Leipzig, 1921; Vol. II.

(29) Henry, D. C. The Cataphoresis of Suspended Particles. Part I. The Equation of Cataphoresis. *Proceedings of the Royal Society A: Mathematical, Physical and Engineering Sciences* **1931**, *133*, 106–129.

(30) Prieve, D. C.; Anderson, J. L.; Ebel, J. P.; Lowell, M. E. Motion of a particle generated by chemical gradients. Part 2. Electrolytes. *Journal of Fluid Mechanics* **1984**, *148*, 247–269.

(31) Anderson, J. L. Colloid Transport by Interfacial Forces. *Annual Review of Fluid Mechanics* **1989**, *21*, 61 99.

(32) O'Brien, R. W.; White, L. R. Electrophoretic mobility of a spherical colloidal particle. *Journal of the Chemical Society, Faraday Transactions 2: Molecular and Chemical Physics* **1978**, *74*, 1607–1626.

(33) Ebel, J. P.; Anderson, J. L.; Prieve, D. C. Diffusiophoresis of latex particles in electrolyte gradients. *Langmuir* **1988**, *4*, 396–406.

(34) Staffeld, P. O.; Quinn, J. A. Diffusion-induced banding of colloid particles via diffusiophoresis 1. Electrolytes. *Journal of Colloid and Interface Science* **1989**, *130*, 69–87.

(35) Warren, P. B. Non-Faradaic Electric Currents in the Nernst-Planck Equations and Nonlocal Diffusiophoresis of Suspended Colloids in Crossed Salt Gradients. *Physical review letters* **2020**, *124*, 248004.

(36) Malkin, E. S.; Dukhin, A. S. Interaction of dispersed particles in an electric field and linear concentration polarization of the double layer. *Colloid Journal of the USSR* **1982**, *44*, 801–810.

(37) Tricoli, V.; Orsini, G. Electrodiffusiophoresis of a large-zeta-potential particle in weak fields. *Journal of Physics: Condensed Matter* **2015**, *27*, 415102.

(38) Yoon, J.; Cho, Y.; Lee, J. H.; Chung, S. Tunable sheathless microfluidic focusing using ion concentration polarization. *Applied Physics Letters* **2015**, *107*, 083507.

(39) Cevheri, N.; Yoda, M. Electrokinetically driven reversible banding of colloidal particles near the wall. *Lab on a Chip* **2014**, *14*, 1391–1394.

(40) Jeon, H.; Lee, H.; Kang, K. H.; Lim, G. Ion concentration polarization-based continuous separation device using electrical repulsion in the depletion region. *Scientific Reports* **2013**, *3*, 3483.

(41) Davies, C. D.; Yoon, E.; Crooks, R. M. Continuous Redirection and Separation of

Microbeads by Faradaic Ion Concentration Polarization. *ChemElectroChem* **2018**, *5*, 877–884.

(42) Davies, C. D.; Crooks, R. M. Focusing, sorting, and separating microplastics by serial faradaic ion concentration polarization. *Chemical Science* **2020**, *11*, 5547–5558.

(43) Gong, M. M.; Nosrati, R.; Gabriel, M. C. S.; Zini, A.; Sinton, D. Direct DNA Analysis with Paper-Based Ion Concentration Polarization. *Journal of the American Chemical Society* **2015**, *137*, 13913–13919.

(44) Wu, Z.-Y.; Ma, B.; Xie, S.-F.; Liu, K.; Fang, F. Simultaneous electrokinetic concentration and separation of proteins on a paper-based analytical device. *RSC Advances* **2017**, *7*, 4011–4016.

(45) Gumuscu, B.; Haase, A. S.; Benneker, A. M.; Hempenius, M. A.; Berg, A. v. d.; Lammertink, R. G. H.; Eijkel, J. C. T. Desalination by Electrodialysis Using a Stack of Patterned Ion-Selective Hydrogels on a Microfluidic Device. *Advanced Functional Materials* **2016**, *26*, 8685–8693.

(46) Rath, M.; Weaver, J.; Wang, M.; Woehl, T. pH-Mediated Aggregation-to-Separation Transition for Colloids Near Electrodes in Oscillatory Electric Fields. *Langmuir* **2021**, *37*, 9346–9355.

(47) Sidelman, N.; Cohen, M.; Kolbe, A.; Zalevsky, Z.; Herrman, A.; Richter, S. Rapid Particle Patterning in Surface Deposited Micro-Droplets of Low Ionic Content via Low-Voltage Electrochemistry and Electrokinetics. *Scientific Reports* **2015**, *5*, 13095.

(48) Silvera Batista, C. A.; Rezvantalab, H.; Larson, R. G.; Solomon, M. J. Controlled Levitation of Colloids through Direct Current Electric Fields. *Langmuir* **2017**, *33*, 10861 – 10867.

(49) Doneux, T.; Bouffier, L.; Goudeau, B.; Arbault, S. Coupling Electrochemistry with Fluorescence Confocal Microscopy To Investigate Electrochemical Reactivity: A Case Study with the Resazurin-Resorufin Fluorogenic Couple. *Analytical Chemistry* **2016**, *88*, 6292 – 6300.

(50) Miomandre, F.; Lépicier, E.; Munteanu, S.; Galangau, O.; Audibert, J. F.; Méallet-Renault, R.; Audebert, P.; Pansu, R. B. Electrochemical Monitoring of the Fluorescence Emission of Tetrazine and Bodipy Dyes Using Total Internal Reflection Fluorescence Microscopy Coupled to Electrochemistry. *ACS Applied Materials & Interfaces* **2011**, *3*, 690 – 696.

(51) Rudd, N. C.; Cannan, S.; Bitziou, E.; Ciani, I.; Whitworth, A. L.; Unwin, P. R. Fluorescence Confocal Laser Scanning Microscopy as a Probe of pH Gradients in Electrode Reactions and Surface Activity. *Analytical Chemistry* **2005-10**, *77*, 6205 – 6217.

(52) Leenheer, A. J.; Atwater, H. A. Imaging Water-Splitting Electrocatalysts with pH-Sensing Confocal Fluorescence Microscopy. *Journal of The Electrochemical Society* **2012**, *159*, H752–H757.

(53) Fuladpanjeh-Hojaghan, B.; Elsutohy, M. M.; Kabanov, V.; Heyne, B.; Trifkovic, M.; Roberts, E. P. L. In-Operando Mapping of pH Distribution in Electrochemical Processes. *Angewandte Chemie* **2019**, *131*, 16971–16975.

(54) Han, J.; Burgess, K. Fluorescent Indicators for Intracellular pH. *Chemical Reviews* **2010**, *110*, 2709–2728.

(55) Cielen, E.; Stobiecka, A.; Tahri, A.; Hoornaert, G. J.; Schryver, F. C. D.; Gallay, J.; Vincent, M.; Boens, N. Synthesis and characterisation of Thio-H, a new excitation and emission ratioable fluorescent Ca 2+ /Mg 2+ indicator with high brightness. *Journal of the Chemical Society, Perkin Transactions 2* **2002**, *0*, 1197–1206.

(56) López-León, T.; Jódar-Reyes, A. B.; Bastos-González, D.; Ortega-Vinuesa, J. L. Hofmeister Effects in the Stability and Electrophoretic Mobility of Polystyrene Latex Particles. *The Journal of Physical Chemistry B* **2003**, *107*, 5696 – 5708.

(57) Suzurikawa, J.; Nakao, M.; Kanzaki, R.; Takahashi, H. Microscale pH gradient generation by electrolysis on a light-addressable planar electrode. *Sensors and Actuators B: Chemical* **2010**, *149*, 205–211.

(58) Obata, K.; Krol, R. v. d.; Schwarze, M.; Schomäcker, R.; Abdi, F. F. In situ observation of pH change during water splitting in neutral pH conditions: impact of natural convection driven by buoyancy effects. *Energy & Environmental Science* **2020**, *13*, 5104–5116.

(59) Wang, Y.; Zhao, L.; Zhao, Y.; Wang, W. Y.; Liu, Y.; Gu, C.; Li, J.; Zhang, G.; Huang, T. J.; Yang, S. Electrocarving during Electrodeposition Growth. *Advanced Materials* **2018**, *30*, 1805686.

(60) Żurawik, T. M.; Pomorski, A.; Belczyk-Ciesielska, A.; Goch, G.; Niedźwiedzka, K.; Kucharczyk, R.; Kreżel, A.; Bal, W. Revisiting mitochondrial pH with an improved algorithm for calibration of the ratiometric 5 (6)-carboxy-SNARF-1 probe reveals anticooperative reaction with H+ ions and warrants further studies of organellar pH. *PloS one* **2016**, *11*, e0161353.

(61) Shi, N.; Nery-Azevedo, R.; Abdel-Fattah, A. I.; Squires, T. M. Diffusiophoretic Focusing of Suspended Colloids. *Physical Review Letters* **2016**, *117*, 258001.

(62) Prieve, D. C. Changes in zeta potential caused by a dc electric current for thin double layers. *Colloids and Surfaces A: Physicochemical and Engineering Aspects* **2004-12**, *250*, 67 – 77.

(63) Chung, Y.-C.; Hsu, J.-P.; Tseng, S. Electrodiffusioosmosis in a solid-state nanopore

connecting two large reservoirs: Optimum pore size. *The Journal of Physical Chemistry C* **2014**, *118*, 19498–19504.

(64) Ristenpart, W. D.; Aksay, I. A.; Saville, D. A. Electrically driven flow near a colloidal particle close to an electrode with a faradaic current. *Langmuir* **2007**, *23*, 4071 4080.

(65) Amrei, S. M. H. H.; Bukosky, S. C.; Rader, S. P.; Ristenpart, W. D.; Miller, G. H. Oscillating Electric Fields in Liquids Create a Long-Range Steady Field. *Physical Review Letters* **2018**, *121*, 185504.

(66) Wirth, C. L.; Rock, R. M.; Sides, P. J.; Prieve, D. C. Single and pairwise motion of particles near an ideally polarizable electrode. *Langmuir* **2011**, *27*, 9781 – 9791.

Graphical TOC Entry